Tetramode metamaterials as phonon polarizers

M.F. Groß*, J.L.G. Schneider*, Y. Wei*, Y. Chen, S. Kalt, M. Kadic, X. Liu, G. Hu[†], and M. Wegener[†]

M.F. Groß, Y. Chen, M. Wegener, M. Kadic

Institute of Nanotechnology, Karlsruhe Institute of Technology (KIT), Karlsruhe 76128, Germany.

M.F. Groß, J.L.G. Schneider, Y. Chen, S. Kalt and M. Wegener

Institute of Applied Physics, Karlsruhe Institute of Technology (KIT), Karlsruhe 76128, Germany.

Y. Wei, X. Liu and G. Hu[†]

School of Aerospace Engineering, Beijing Institute of Technology (BIT), Beijing 100811, China.

M. Kadic

Institut FEMTO-ST, UMR 6174, CNRS, Université de Bourgogne Franche-Comté (UBFC), Besançon 25030, France.

* These authors have contributed equally to this work.

E-mail: (hugeng@bit.edu.cn (G.H.); martin.wegener@kit.edu (M.W.))

Abstract:

In classical Cauchy elasticity, three-dimensional materials exhibit six eigenmodes of deformation. Following the 1995 work of Milton and Cherkaev, extremal elastic materials can be classified by the number of eigenmodes, N, out of these six that are "easy". Using Greek number words, this leads to hexamode ($N = 6$), pentamode ($N = 5$), tetramode ($N = 4$), trimode ($N = 3$), dimode ($N = 2$), and monomode ($N = 1$) materials. While hexamode materials are unstable in all regards, the possibility of pentamode metamaterials ("meta-fluids") has attracted considerable attention throughout the last decade. Here, inspired by the 2021 theoretical work of Wei, Liu, and Hu, microstructured three-dimensional polymer-based tetramode metamaterials are designed and characterized by numerical band-structure calculations, fabricated by laser printing, characterized by ultrasound experiments, and compared to the theoretical ideal. An application in terms of a compact and broadband polarizer for acoustical phonons at ultrasound frequencies is demonstrated.

Keywords: metamaterials, phonons, elastic waves, polarization, ultrasound experiments, tetramode materials

1. Introduction

According to Hooke's law,[1] linear elastic materials react with a deformation, the amplitude of which is proportional to the amplitude of the force field exerted onto them. The generalization of the one-dimensional Hooke's spring constant to three-dimensional materials leads to the classical Cauchy elasticity tensor.[1, 2] In three dimensions, this elasticity tensor can be represented by a 6×6 matrix (in Voigt notation).[1, 2] Therefore, Cauchy elastic materials generally exhibit six orthogonal eigenmodes of deformation. For special extremal cases, some of the corresponding eigenvalues may be very small compared to the others or even zero. This means that these eigenmodes are "easy" in the sense that no force or energy is required to induce the corresponding deformation.[3] The number of easy eigenmodes, $N = 1, 2, 3, 4, 5$, and 6, can be used to name extremal materials in Cauchy elasticity.[3-6] Using Greek number words, this leads to hexamode ($N = 6$), pentamode ($N = 5$), tetramode ($N = 4$), trimode ($N = 3$), dimode ($N = 2$), and monomode ($N = 1$) materials. While hexamode materials correspond to the absence of an elastic material and are hence trivial, the other five classes of extremal elastic materials potentially provide us with unusual and interesting mechanical properties.

About a decade ago, following a theoretical suggestion by Milton and Cherkaev,[3] man-made architectures called pentamode metamaterials were introduced experimentally.[7] Ideally, five of their elastic eigenmodes have strictly zero eigenvalues. In practice, the eigenvalue of one eigenmode is orders of magnitude larger than that of the other five eigenmodes. This behavior was achieved by approximating ideal hinges within a diamond-like lattice by thin connections between double-cone elements.[7, 8] In this manner, the compression of all double-cone elements is uneasy, whereas all other material deformations are easy. This equivalently means that the wave speed of longitudinally polarized phonons is much (ideally infinitely) larger than the wave speed of all transverse acoustical phonons, leading to a broad frequency interval in which only longitudinal phonons can propagate.[8-10] Propagating transverse acoustical phonons are forbidden in this interval. Such behavior can be used for cloaking[11-14] or as a longitudinal polarizer[9]. As usual[15], transverse (longitudinal) phonons mean that the phonon displacement-vector $\vec{u}$ is polarized perpendicular (parallel) to the phonon wavevector $\vec{k}$.

Such pentamode longitudinal elastic polarizer is distinct from a linear polarizer in optics, for which one transverse polarization is transmitted, whereas the orthogonal transverse polarization is suppressed.[16-18] Longitudinal waves are usually absent in optics. Polarizers in optics can be realized by exploiting birefringent materials[19]. For example, a birefringent metamaterial can be constructed by a grid of parallel conducting metal wires with sub-wavelength spacing. Such grid polarizers are used in many commercial Fourier-transform spectrometers from the visible to the far-infrared of the electromagnetic spectrum.[18] According to the classification of Milton and Cherkaev[3], such an array of conductive metal wires (cf. Figure 1 in Reference[18]) corresponds to a dimode metamaterial in electrical conduction (they spoke of a "bimode" metamaterial). Electrical conduction in three dimensions is conceptually much simpler than elasticity[2] because one has only three orthogonal eigenmodes (rather than six in Cauchy elasticity).

Here, building on previous theoretical work on tetramode metamaterials (called "quadramode" metamaterials there),[20, 21] we present theory and experiments on tetramode elastic metamaterials. These unusual microstructured man-made materials are realized by tailored three-dimensional lattices composed of double-cone elements with small (ideally zero) diameter d at the points where the cone tips merge into small spheres connecting the cones. As an application, we show that tetramode metamaterials can be used as broadband polarizers for transverse metamaterial phonons.

2. Metamaterial design and phonon bands

Figure 1 illustrates the architecture of the tetramode metamaterial considered in this work. It is composed of only a single Cauchy-elastic constituent material and voids within. This constituent is shaped into double-cone elements that are arranged into a metamaterial unit cell that is placed onto a simple-cubic translation lattice with lattice constant a. A tetragonal symmetry metamaterial crystal results. The crucial geometrical parameter of this tetramode metamaterial architecture is the size or diameter, d, of the regions where the tips of different cones merge into the small spheres with diameter $2r$ connecting the cones (see inset in Figure 1). In our previous work on pentamode metamaterials,[7-9] we did not use such small spheres but rather connected the cone tips directly. Here, we use the union of spheres and several cone tips to obtain a geometrically well-defined object. Furthermore, the spheres make the structure more tolerant against fabrication imperfections, for example if the cone tips do not meet perfectly in one point. In the case of $2r > d$ or even $2r \gg d$, the shear stiffness of the connection is still mainly determined by d and only weakly depends on $2r$. The larger diameter at the thick ends of the cones is $D > d$. Clearly, the period a merely scales the frequency and the wavenumber, such that the dimensionless parameters determining the qualitative behavior of the tetramode metamaterial are the three ratios d/a, $2r/a$, and D/a.

An ideal effective tetramode material results if one considers the limit $d/a \to 0$ for the structure in Figure 1. This statement is illustrated by the numerical band-structure calculations (see Methods) depicted in Figure 2. In the three columns of Figure 2, we show three different band structures, for three different ratios of d/a, versus the wavenumber k_z with $\vec{k} = (0,0,k_z)$. This phonon propagation direction refers to the below experiments. Phonon band structure along the usual tour of the wave vector $\vec{k} = (k_x, k_y, k_z)$ through the high-symmetry points (see inset) of the Brillouin zone of the simple-cubic lattice (which is not the Wigner-Seitz cell of the tetramode metamaterial crystal, cf. Figure 1) are shown in Figure S3. In Figure 2, the relevant bands are colored and labeled as x, y and z, corresponding to the dominant polarization direction of the displacement-vector field. Since for every mode, the displacement polarization is not pure, the designation as x-like, y-like or z-like is arguably more appropriate but is omitted for the sake of brevity. From the panels of Figure 2, it becomes clear that the maximum frequency of the two lowest bands is shifted to significantly smaller values as the ratio d/a decreases, compared to the maximum frequency of the third lowest band. As a result, the relative frequency range in which only the x-polarized transverse phonon mode can propagate becomes larger as the ratio d/a decreases. To allow for direct comparison with the static elastic properties, we retrieve the effective elasticity matrix of the three cases in Figure 2 from fitting the dispersion relations in the long-wavelength limit (see Supporting Information). Their corresponding six eigenvalues are also shown in the middle row of Figure 2. As expected from the definition of the tetramode metamaterials, four out of the six eigenvalues are at least one order of magnitude smaller than the other two.

To further explain the results in Figure 2, Figure S1(a) illustrates how the metamaterial unit cell can support a finite shear stress along the x-direction. In contrast, Figure S1(b) shows that the architecture cannot support a shear stress along the y-direction. Likewise, it cannot support a normal stress along the z-direction. As a result, elastic waves with y- and z-polarization of the displacement-vector become evanescent for frequencies larger than the maximum frequency of the corresponding bands in Figure 2, whereas waves polarized along the x-direction are still propagating and are transmitted. This combination leads to a polarizer action that extracts from an arbitrary incident elastic wave with wave vector $\vec{k} = (0,0,k_z)$ (cf. Figure 1) and displacement-vector $\vec{u}_{in} = (u_x, u_y, u_z)$ the transverse component with x-polarization, i.e., $\vec{u}_{out} = (u_x, 0, 0)$ for all inputs. The measurements to be presented below directly record $\vec{u}_{in}$ and $\vec{u}_{out}$ in real space and real time.

3. Comparison between experiment and numerical results

We have manufactured the samples for these experiments by 3D laser printing (see Methods) using a commercial instrument (Nanoscribe, Photonics Professional GT) and a commercial photoresist (Nanoscribe, IP-S). Each sample is composed of $9 \times 6 \times 6$ unit cells. A gallery of optical and electron micrographs with different magnifications and different viewing angles onto the polymer tetramode metamaterials is depicted in Figure. 3. The targeted geometrical parameters (cf. Figure. 1) are: $d = 4\,\mu m$, $D = 16\,\mu m$, and $a = 200\,\mu m$, hence $d/a = 0.02$. Yet smaller ratios of d/a would be desirable, but are not accessible due to the limited spatial resolution of the 3D laser printer. Figure 3 also includes a 3D rendered representation of experimental data acquired by confocal laser-scanning optical fluorescence microscopy (Zeiss, LSM980), showing a single tetramode metamaterial unit cell. Overall, the panels of Figure 3 evidence very high sample quality despite the considerable complexity of the tetramode architecture. However, certain imperfections are visible in Figure 3(d). This especially concerns the critical regions in which the cones merge with the spheres (see discussion above). While the cone cross section should be circular where cones and spheres meet, it is actually somewhat elliptical due to the imperfectly compensated ellipticity of the laser focus point-spread function in the 3D laser printer. We have been unable to eliminate these sample imperfections. In fact, it was hard to arrive at the level of quality apparent from Figure 3. Therefore, we rather account for the remaining sample imperfections in the theoretical modelling when comparing experimental and theoretical results below (also see Figure S3).

The experiments presented in Figure 4 and 5 are conceptually simple, yet technologically demanding. The tetramode metamaterial samples are glued onto piezoelectric actuator assemblies, which are showcased in Figure 4(b) and Figure 4(e). By applying a time-harmonic voltage to the respective actuator at variable angular frequency ω, with $\omega/(2\pi)$ from 0 up to 300 kHz, it reacts with a time-harmonic displacement-vector field at the interface between actuator and metamaterial sample. This constitutes the input displacement $\vec{u}_{in} = (u_x, u_y, u_z)$. Generally, depending on the frequency, all three components are nonzero. We measure the local input displacement $\vec{u}_{in} = (u_x, u_y, u_z)$ as well as the local output displacement $\vec{u}_{out} = (u_x, 0,0)$ in real time by a dedicated optical setup (see Methods and Supporting Information). This setup allows for measuring the components u_x and u_y by optical confocal image acquisition and subsequent digital image cross-correlation analysis.[22] The measurement of the u_z component is conducted by laser Doppler vibrometry.[23] The latter has not previously been used by us.

In the experiments, two actuator orientations for the excitation of elastic waves are chosen. In the first orientation, the main actuator axis is aligned with the sample *z*-axis and in the second orientation along the sample *y*-axis. The intention behind these orientations is to better showcase the sample performance as a larger input displacement can naturally result in a larger measurable suppression of the unwanted displacement polarization.

Examples for the frequency of $\omega/(2\pi) = 180$ kHz are shown in Figure 4. Here, the measured displacement trajectories, taken at the locations highlighted in red and blue respectively, are shown next to several oblique-view micrographs of the tetramode metamaterial sample.

The input displacement trajectories (red boxes) contain significant components along all three spatial directions, whereas the output displacement trajectory (blue boxes) on the sample top center exhibit $u_y(t)$ and $u_z(t)$ components versus time t, the amplitudes of which are very small compared to that of $u_x(t)$. This behavior corresponds to the anticipated polarizer action. We have also recorded the output displacement trajectories at other positions closer to the sample's edges (not depicted). We find that the polarizer behavior deteriorates due to edge effects, which correspond to a large number of back-folded bands in the band structure of the tetramode metamaterial beam with finite cross section shown in Figure 3(c) and Figure 4(a). Therefore, in what follows, we concentrate on measuring the output displacement

trajectory in the middle of the top of the sample. If larger usable areas should be required in an application, the tetramode metamaterial sample footprint would need to be increased.

Figure 5 summarizes the results of experiments as the example shown in Figure 4, but for many different excitation frequencies. For reference, we depict in the left column band structures for tetramode metamaterial beams that are infinitely periodic along the z-axis (also cf. Figure 2). The right-hand side column refers to our experiments, which are compared to numerical calculations shown in the middle column of Figure 5. For the experiment, the displacement ratios versus frequency show a suppression of the unwanted u_y component of about two orders of magnitude (highlighted by the light green area) for frequencies above 50 kHz. The unwanted u_z component is suppressed by more than one order of magnitude (see light green area) for frequencies above 120 kHz. Both behaviors are in good agreement with theory, but theory tends to predict even slightly better suppressions. We assign this difference to remaining sample imperfections.

It is interesting to compare the measured broadband-polarizer performance with that of other types of polarizers. The only other published setting that we are aware of and that theoretically allows for separating elastic waves with different polarizations is Reference.[24] There, different refraction angles at an interface for the different polarizations could be used in the sense of a phonon polarizer. However, experiments are elusive. For optical polarizers, suppression usually refers to the ratio of transmitted intensities, which are proportional to the square of the electric field.[25] By analogy, we should square the above mentioned displacement ratios, leading to a suppression of the transverse polarization of about four orders of magnitude. This value is better than that of most wire-grid polarizers used in Fourier-transform spectrometers (see discussion in the introduction). A comparison in regard to the suppression of the longitudinal polarization is not possible because electromagnetic waves are usually transversely polarized.

4. Conclusions

Extremal Cauchy-elastic metamaterials exhibit a certain number of easy modes. Ideally, these are connected to zero force or energy needed for the corresponding deformation. Previous work realized pentamode and monomode elastic metamaterials. Here, we have introduced and realized tetramode elastic metamaterials. We have emphasized dynamic wave properties (rather than static properties) because these allow for using tetramode metamaterials as compact and broadband transverse linear elastic polarizers – the so-far missing counterpart to linear polarizers in optics. Our proof-of-principle findings can be improved systematically by further reducing the d/a ratio (cf. Figure 1 and 2) and/or by introducing more metamaterial unit cells along both, the phonon propagation direction and perpendicular to it.

5. Methods

5.1. Numerical band structure calculations

Phonon band-structures (c.f. Figure 2) for the tetramode metamaterials are numerically obtained by using the Solid Mechanics Module of the commercial software package COMSOL Multiphysics. Bloch-periodic boundary conditions are applied to the six surfaces of the cubic unit cell (cf. Figure 1). All other boundaries are stress free. The solved mathematical equations for the linear elastic-wave propagation problem are provided in the Supporting Information (cf. Equation (S1)). For the band structures depicted in Figure 2, we only sweep the Bloch wave vector $\vec{k} = (0, 0, k_z)$ from $(0, 0, 0)$ to $(0, 0, \pi/a)$. More complete results for tetramode metamaterials are shown in Figure S3. There, we consider the usual tour of wave vectors along high-symmetry directions through the first Brillouin zone of the simple-cubic lattice.

5.2. Tetramode sample fabrication

The tetramode metamaterial samples are fabricated by 3D laser microprinting (Professional GT, Nanoscribe). A 25 × objective lens with a numerical aperture of 0.8 (Carl Zeiss) is dipped into the liquid photoresist (IP-S, Nanoscribe). The laser focus is scanned by two galvanometric mirrors at a focus velocity of 0.110 m/s. The mean laser power at the entrance pupil of the objective lens is set to 37.5 mW. The 3D model of the sample is created with a commercial software package COMSOL Multiphysics (COMSOL Inc.). The model is processed with the commercial software Describe (Nanoscribe) to generate machine code for the 3D laser printer. A hatching distance of 300 nm and a slicing distance of 500 nm are chosen. For printing, the model of the unit cell is split up in parts which are printed sequentially. This guarantees well-defined connections between the individual parts and alleviates the fabrication of overhanging sections of the unit cell. Each sample is printed onto a bottom plate with a small handle. This facilitates the manipulation of the samples and ensures proper contact of the samples when glued on a piezoelectric actuator assembly. The bottom plates are written with a focus velocity of 0.140 m/s, a hatching distance of 500 nm and a slicing distance of 1.5 µm. After printing, the samples are rinsed in a beaker of propylene glycol methyl ether acetate (PGMEA) for at least 30 min to remove excess photoresist. To prepare for critical point drying with CO_2 (Leica, EM CPD300), the samples are rinsed again with acetone for about 5 min. Further detail on the printing parameters and the printing sequence can be extracted from the GWL-files included in the data repository and published with this work (https://xxxxxxxxxxxxx).

5.3. Experiment setup

The tetramode sample is glued onto a piezoelectric actuator assembly. The main axis of the piezoelectric actuator (Physik Instrumente, PL055.31 PICMA) is either aligned with the sample y- or z-axis. The sample exceeds the field of view of the optical measurement setup. Therefore, the assembly is mounted on a xyz-translation stage with piezo-inertia drives (Physik Instrumente, Q-545) for manipulation of the sample. For the measurement, the region of interest on the sample is positioned in the focal plane of the microscope objective lens (cf. Figure S4) which results in a top-view of the tetramode sample, along the inverse z-axis. The back-reflected light is measured by two avalanche photodiode modules. The first module (APD1) belongs to the optical confocal imaging mode. It outputs a photovoltage proportional to the incident light power. The second module (APD2) serves the heterodyne laser Doppler vibrometry mode. The output Doppler signal voltage is proportional to the AC-component of the interfering electric fields of the back-reflected light and a frequency shifted reference beam. The frequency shift is generated by an acousto-optic modulator (AA, MT80-A1.5-VIS).

5.4. Single-frequency excitation measurement

The mechanical excitation of the tetramode samples is achieved by driving the piezoelectric actuator with an amplified sinusoidal voltage. The data acquisition units of the optical setup are synchronized to this drive signal to ensure the retrieval of the correct temporal phase information of the measured displacement-vector components.

The data acquisition is split into two channels, corresponding to the optical imaging mode and the laser Doppler vibrometry mode, respectively. For the optical imaging, spatial regions of interest (ROIs) on the excited sample are scanned. Each ROI is divided into 60 × 60 pixels and spans a region of 30 × 30 µm. At every pixel, a time-series of the photovoltage from APD1 is recorded, sequentially. Afterwards, for the laser Doppler vibrometry mode, a time series of the APD2 output voltage is recorded at the central pixel of the current ROI before moving on to the next. In total, four ROIs are measured on every sample. Three ROIs are spaced about 750 µm apart, including cross-shaped markers on the sample bottom plate. After averaging, the data represents the displacement input to the sample. The fourth ROI is located at the sample top center and is considered the displacement output.

The excitation frequency is incremented in steps of $\Delta f = 10\,\text{kHz}$ from 0 to 300 kHz and is held constant until all ROIs on the sample are measured for that frequency. A buffer of about 200 ms in the data acquisition is included between switching of the excitation frequency. This ensures that the sample has sufficient time to respond to the new excitation.

To form images for the digital image cross-correlation analysis, the time series are combined while considering the synchronization between data acquisition and the drive signal[22] (cf. Figure S5). The demodulation and digital signal processing for the laser Doppler vibrometry is implemented as a digital IQ-demodulator using the arctangent phase method (cf. Figure S6).[26]

Supporting Information

Supporting Information is available from the Wiley Online Library or from the authors.

Conflict of interests

Authors declare that they have no competing interests.

Data and code availability

The data that support the plots within this paper and other findings of this study are available from the corresponding authors upon reasonable request and are published on the open access data repository of the Karlsruhe Institute of Technology [Enter repository].
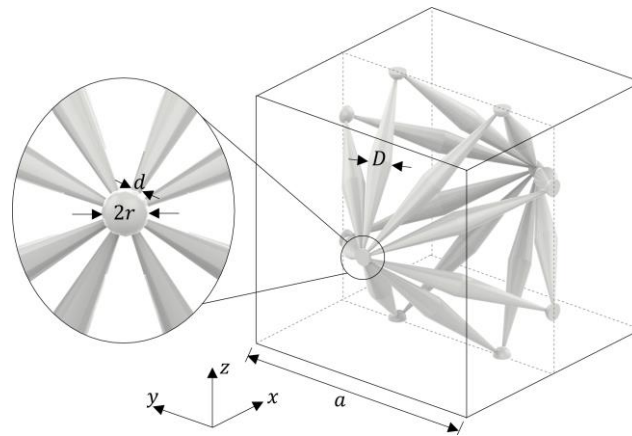
Figures and captions:

Figure 1. 3D model of the tetramode sample unit cell. The unit cell exhibits tetragonal symmetry and placed onto a simple-cubic translation lattice with lattice constant a. The unit cell is constructed from double-cone elements connected by spheres of radius r. The crucial design parameters D and d are the diameter of the double-cone center and the diameter of the connection between double-cones and spheres, respectively. The spheres are chosen as connection-hubs for the double-cone elements to obtain a well-defined geometry and to facilitate sample fabrication and the subsequent characterization using optical-image digital cross-correlation analysis and laser Doppler vibrometry. For the constitute material, we choose the parameters of Young's modulus $E = 4.19$ GPa, Poisson's ratio $v = 0.4$, and mass density $\rho = 1190 \text{ kg} \cdot \text{m}^{-3}$ for the numerical calculations.
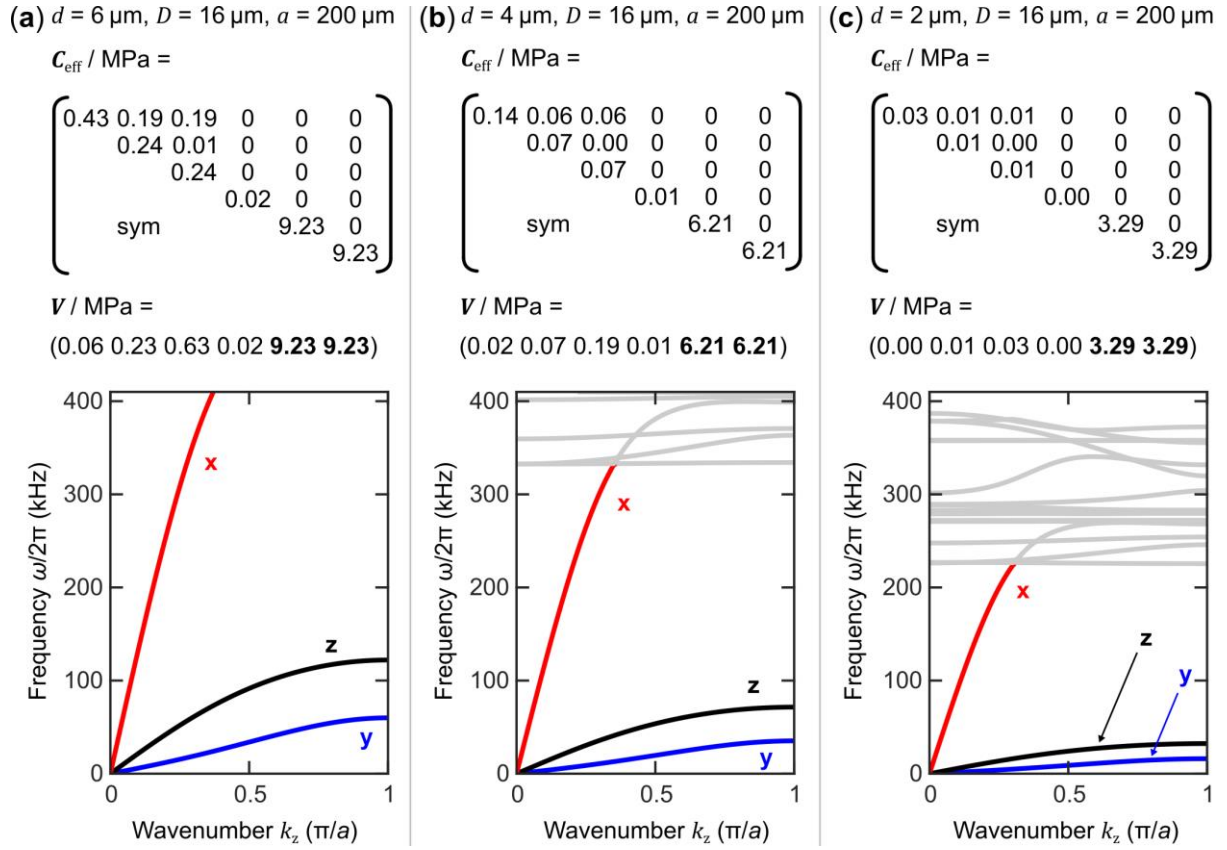
(a) $d = 6\ \mu m$, $D = 16\ \mu m$, $a = 200\ \mu m$

$\boldsymbol{C}_{\text{eff}}$ / MPa =

$$\begin{bmatrix} 0.43 & 0.19 & 0.19 & 0 & 0 & 0 \\ & 0.24 & 0.01 & 0 & 0 & 0 \\ & & 0.24 & 0 & 0 & 0 \\ & & & 0.02 & 0 & 0 \\ & \text{sym} & & & 9.23 & 0 \\ & & & & & 9.23 \end{bmatrix}$$

$\boldsymbol{V}$ / MPa =

(0.06 0.23 0.63 0.02 **9.23 9.23**)

(b) $d = 4\ \mu m$, $D = 16\ \mu m$, $a = 200\ \mu m$

$\boldsymbol{C}_{\text{eff}}$ / MPa =

$$\begin{bmatrix} 0.14 & 0.06 & 0.06 & 0 & 0 & 0 \\ & 0.07 & 0.00 & 0 & 0 & 0 \\ & & 0.07 & 0 & 0 & 0 \\ & & & 0.01 & 0 & 0 \\ & \text{sym} & & & 6.21 & 0 \\ & & & & & 6.21 \end{bmatrix}$$

$\boldsymbol{V}$ / MPa =

(0.02 0.07 0.19 0.01 **6.21 6.21**)

(c) $d = 2\ \mu m$, $D = 16\ \mu m$, $a = 200\ \mu m$

$\boldsymbol{C}_{\text{eff}}$ / MPa =

$$\begin{bmatrix} 0.03 & 0.01 & 0.01 & 0 & 0 & 0 \\ & 0.01 & 0.00 & 0 & 0 & 0 \\ & & 0.01 & 0 & 0 & 0 \\ & & & 0.00 & 0 & 0 \\ & \text{sym} & & & 3.29 & 0 \\ & & & & & 3.29 \end{bmatrix}$$

$\boldsymbol{V}$ / MPa =

(0.00 0.01 0.03 0.00 **3.29 3.29**)

Figure 2. Calculated effective elasticity matrix $\boldsymbol{C}_{\text{eff}}$ (in Voigt notation), the respective set of eigenvalues $\boldsymbol{V}$, and the band structure when varying the critical parameter d, the connection diameter between double-cones and spheres (**a** to **c**). The numeric values are rounded to the second digit. Calculations are performed for an infinite sample and are detailed in the Supporting Information. For all parameter choices of d, two out of six eigenvalues are at least one order of magnitude larger than the other eigenvalues. Furthermore, in the band structures, it can be seen how the variation of d influences the maximum frequency of the red and the black or blue bands. Smaller values of d increase the ratio between the maximum frequency of the red band and the respective maximum frequency of the black or blue band. This can also be inferred from the slope of the bands. Reducing d reduces the slope of the two lowest i.e. black and blue bands, while the slope of the third lowest red band remains almost constant. In these plots, the red and the blue band correspond to transverse waves polarized along the x- or y-axis and the black band to the longitudinal wave polarized along the z-axis. The parameters in panel (**b**) are chosen for the fabrication of the finite-size metamaterial samples.
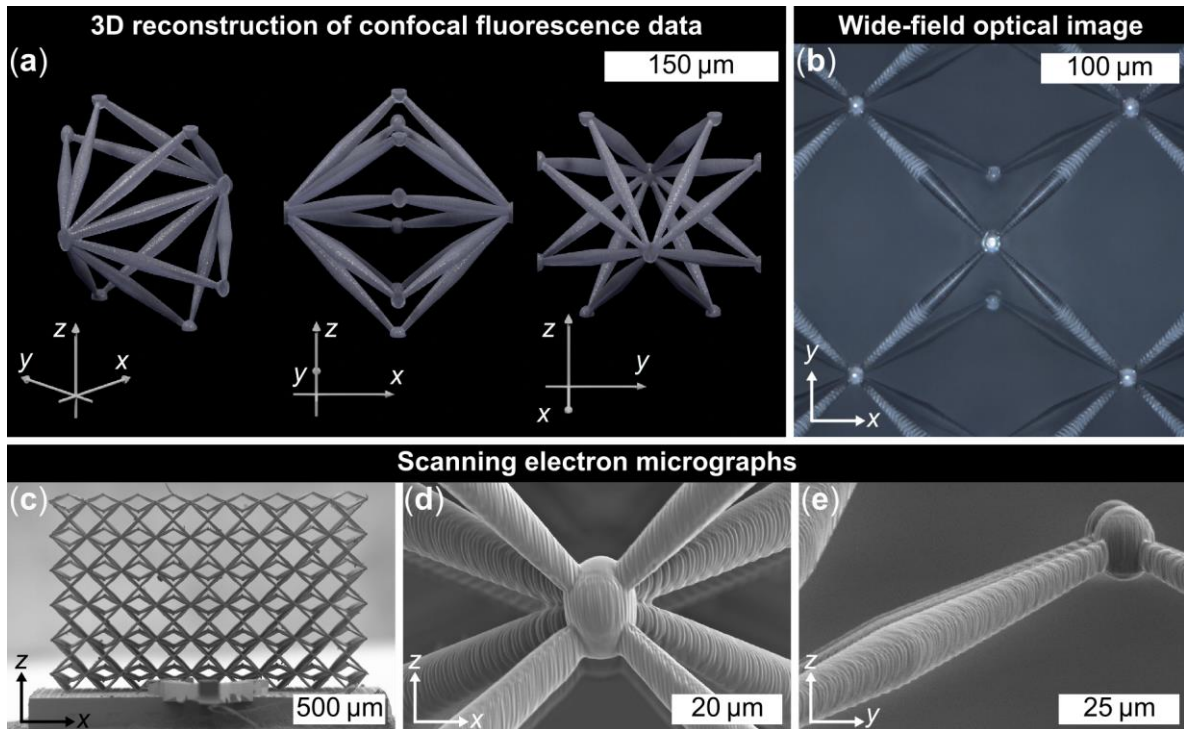
Figure 3. Showcase of different sample features. (**a**) 3D iso-intensity surface of a single unit cell acquired with a laser-scanning confocal fluorescence optical microscope (LSM980, Zeiss) using the autofluorescence of the polymer. Coloring and post-processing was performed in ImageJ and Blender. (**b**) Close-up wide-field image of a sample using the extended-depth-of-field feature of a wide-field optical microscope (Smartzoom 5, Zeiss), when imaging along the inverse z-axis. A specular reflection from the LED-illumination can be seen in the center as a bright spot. This specular reflection is beneficial for the laser-Doppler vibrometry analysis. (**c** to **e**) Scanning-electron micrographs. (**c**) Side-view of the sample on its bottom plate. The sample shows 9 unit cells along the x- and 6 unit cells along the y- and z-direction. Due to the viewing-angle, the cells in y-direction are not visible. (**e**) Connection of two neighboring unit cells. The anisotropic 3D printing voxel elongates the desired sphere to an ellipsoid. (**d**) Close-up of the region showing the two critical sample parameters, namely the diameter D in the double-cone center and d on the spheres connecting to the cones.
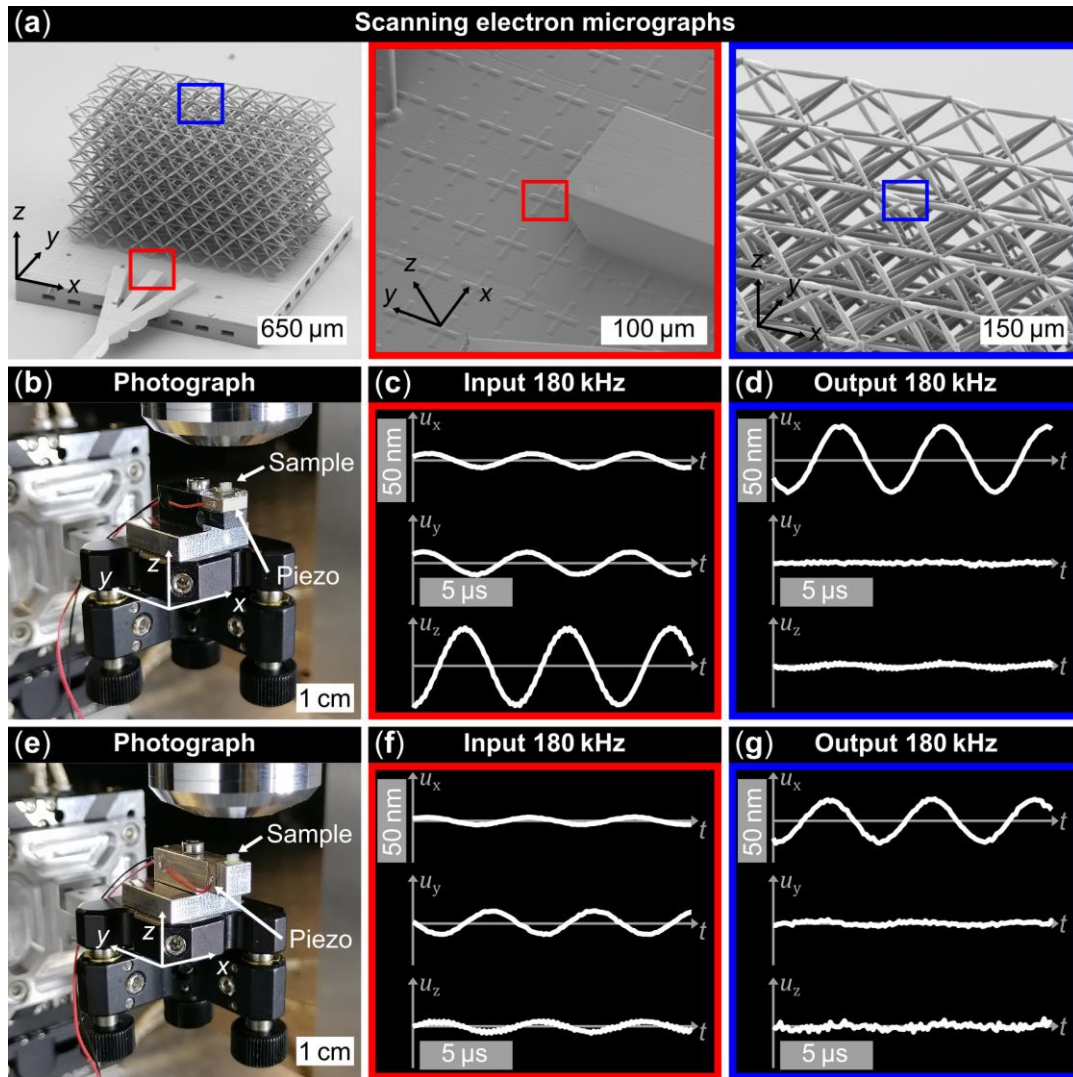
Figure 4. Measurement assemblies and exemplary data sets exhibiting the polarizer functionality. (**a**) Scanning electron micrographs of the sample with the locations highlighted which we consider as displacement input (red box) on the sample bottom plate, and output (blue box) at a central location on the sample top. (**b**) Photograph of the sample assembly in the measurement setup. The microscope objective lens can be seen at the top. A mirror mount is used as a tilt-correction platform for the sample under the objective lens. The sample is glued onto a silica glass substrate which in turn is glued to a piezoelectric actuator (from which cables emerge). The actuator is glued to a PVC mount with the main actuator axis aligned along the sample y-axis. (**c**) Time-resolved evolution of the displacement-vector components as an input to the sample. The x- and y-components of the displacement-vector were obtained by optical-image digital cross-correlation analysis. The z-component was obtained using laser Doppler vibrometry. Due to the orientation of the actuator, the input displacement along the z-axis is the largest. (**d**) Corresponding time-resolved displacement output at the sample top. From the displacement raw data, it can be clearly seen how displacements along the y- and z-axis are suppressed and only a significant displacement along the x-axis is left at the sample top. The temporal phase delay between input and output originate from damping within the polymer. The output displacement can exceed the input displacement due to back reflection of the waves at the top of the sample. (**e** to **g**) Similar example shown for an assembly where the actuator is glued onto an aluminum mount and with the main actuator axis is aligned with the sample y-axis. To achieve this orientation, the sample is glued onto an aluminum cuboid which serves as an elbow piece.
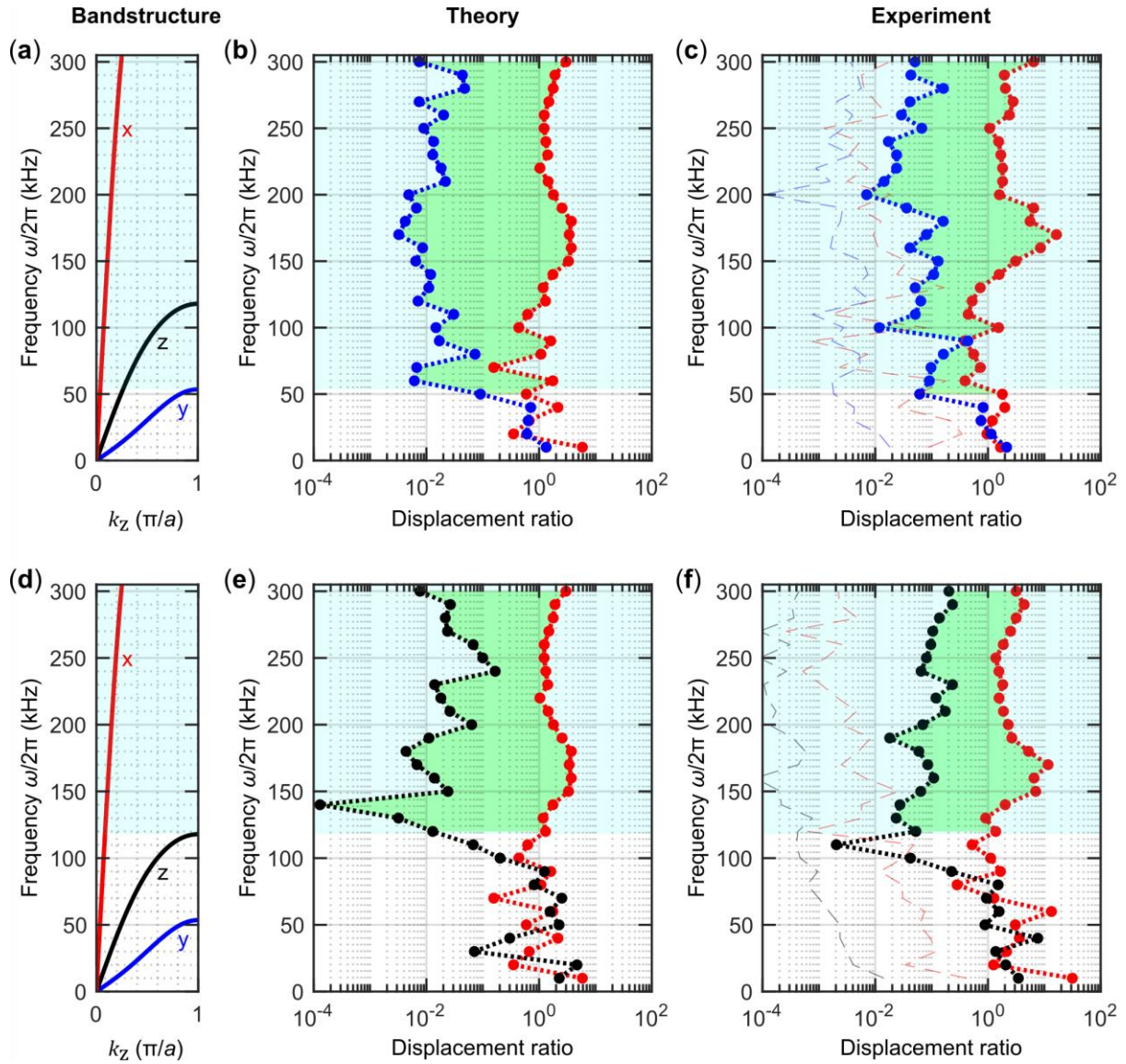
Figure 5. Results as in Figure 4, but shown versus excitation frequency. (**a** and **d**) Band structure for waves propagating along the sample z-axis with wave number k_z in an infinite beam. The red and the blue band correspond to transverse waves polarized along the x- or y-axis and the black band to the longitudinal wave polarized along the z-axis. The frequency region of the gap between the (**a**) x- and y-polarized or (**c**) x- and z-polarized modes is highlighted in light blue, respectively. (**b** and **e**) Displacement ratios computed from theory for the ratio of the excitation displacement-vector components on the sample bottom plate to the vector components of the central point on the sample top. To emphasize the predicted polarizer behavior of the sample, the area between the curves is shaded in light green. (**c** and **f**) Experimental results for the corresponding displacement ratios. Data from panel (**c**) was obtained by aligning the piezoelectric actuator main axis along the sample y-axis and in (**e**) along the sample z-axis. The x- and y-components of the displacement-vector were obtained by optical-image digital cross-correlation analysis. The z-component was obtained using laser Doppler vibrometry. A suppression of up to two orders of magnitude is achieved experimentally, when comparing the displacement ratio of the transmitted x-displacement to the ratio of the suppressed y- and z-displacements. In terms of mechanical power, this corresponds to a suppression of up to four orders of magnitude making it well comparable to a polarizer device in optics. The dashed lines indicate the sensitivity limit of the experimental setup. These lines are obtained by calculating the ratio of the excitation displacement-vector components during measurement to a zero-measurement at the sample top where the piezoelectric actuator is not driven.

Reference

[1]   A. E. H. Love, *A Treatise on the Mathematical Theory of Elasticity*. Cambridge, England: Cambridge University Press **1944**.

[2]   G. W. Milton, *The Theory of Composites*. Cambridge, England: Cambridge University Press **2002**.

[3]   G. W. Milton, A. V. Cherkaev, Which elasticity tensors are realizable?. *Journal of Engineering Materials and Technology* **1995**, 117, 483.

[4]   C. N. Layman, C. J. Naify, T. P. Martin, D. C. Calvo, G. J. Orris, Highly Anisotropic Elements for Acoustic Pentamode Applications. *Physical Review Letters* **2013**, 111, 24302.

[5]   Z. Li, Z. Luo, L. Zhang, C. Wang, Topological design of pentamode lattice metamaterials using a ground structure method. *Materials & Design* **2021**, 202, 109523.

[6]   G. W. Milton, Complete characterization of the macroscopic deformations of periodic unimode metamaterials of rigid bars and pivots. *Journal of the Mechanics and Physics of Solids* **2013**, 61, 1543.

[7]   M. Kadic, T. Bückmann, N. Stenger, M. Thiel, M. Wegener, On the practicability of pentamode mechanical metamaterials. *Applied Physics Letters* **2012**, 100, 191901.

[8]   M. Kadic, T. Bückmann, R. Schittny, M. Wegener, On anisotropic versions of three-dimensional pentamode metamaterials. *New Journal of Physics* **2013**, 15, 023029.

[9]   A. Martin, M. Kadic, R. Schittny, T. Bückmann, M. Wegener, Phonon band structures of three-dimensional pentamode metamaterials. *Physical Review B* **2012**, 86, 155116.

[10]   M. Kadic, T. Bückmann, R. Schittny, P. Gumbsch, M. Wegener, Pentamode metamaterials with independently tailored bulk modulus and mass density. *Physical Review Applied* **2014**, 2, 54007.

[11]   A. N. Norris, Acoustic cloaking theory. *Proceedings of the Royal Society A: Mathematical, Physical and Engineering Sciences* **2008**, 464, 2411.

[12]   T. Bückmann, M. Thiel, M. Kadic, R. Schittny, M. Wegener, An elasto-mechanical unfeelability cloak made of pentamode metamaterials. *Nature Communications*, **2014**, 5, 1.

[13]   Y. Chen, M. Zheng, X. Liu, Y. Bi, Z. Sun, P. Xiang, J. Yang, G. Hu, Broadband solid cloak for underwater acoustics. *Physical Review B* **2017**, 95, 180104.

[14]   A. N. Norris, Acoustic metafluids. *Journal of the Acoustical Society of America* **2009**, 125, 839.

[15]   K. F. Graff, *Wave Motion in Elastic Solids*. North Chelmsford, USA: Courier Corporation **2012**.

[16]   L. Guo, Nanoimprint Lithography: Methods and Material Requirements. *Advanced Materials* **2007**, 19, 495.

[17]   M. Xu, H. Urbach, D. de Boer, H. Cornelissen, Wire-grid diffraction gratings used as

polarizing beam splitter for visible light and applied in liquid crystal on silicon. *Optics Express* **2005**, 13, 2303.

[18] S. Ahn, K. Lee, J. Kim, S. H. Kim, J. Park, S. Lee, P. Yoon, Fabrication of a 50 nm half-pitch wire grid polarizer using nanoimprint lithography. *Nanotechnology* **2005**, 16, 1874.

[19] L. D. Barron, *Molecular light scattering and optical activity*. Cambridge, England: Cambridge University Press, **2004**.

[20] Y. Wei, X. Liu, G. Hu, Quadramode materials: Their design method and wave property. *Materials & Design* **2021**, 210, 110031.

[21] Y. Wei, G. Hu Wave characteristics of extremal elastic materials. *Extreme Mechanics Letters* **2022**, 55, 101789.

[22] J. A. I. Martínez, M. F. Groß, Y. Chen, T. Frenzel, V. Laude, M. Kadic, M. Wegener, Experimental Observation of Roton-Like Dispersion Relations in Metamaterials. *Science Advances* **2021**, **7**, m2189.

[23] C. Rembe and A. Dräbenstedt, Laser-scanning confocal vibrometer microscope: Theory and experiments. *Review of Scientific Instruments* **2006**, 77, 083702.

[24] Liu H., Zhang Q., Zhang K., Hu G., Duan H. Designing 3D digital metamaterial for elastic waves: from elastic wave polarizer to vibration control. *Advanced Science* **2019**, 6, 1900401.

[25] Kim S. Y., Gwyther J., Manners I., Chaikin P. M., Register R. A. Metal-containing block copolymer thin films yield wire grid polarizers with high aspect ratio. *Advanced Materials* **2014**, 26, 791.

[26] C. Rembe, G. Siegmund, H. Steger, M. Wörtge, "Measuring MEMS in Motion by Laser Doppler Vibrometry" in *Optical Inspection of Microsystems*, CRC Press, **2019**, p. 584.

Table of contents
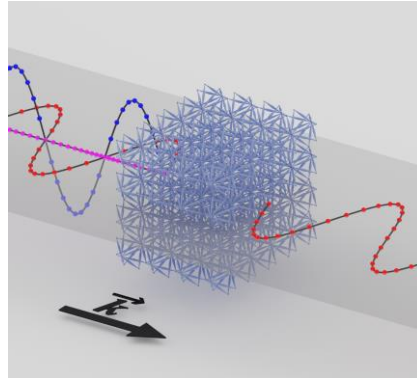
An experimental realization and application of a tetramode material is presented. According to Cauchy elasticity, four out of the six deformation modes of such materials are considered "easy". A property that can be exploited as a compact broadband polarizer for transverse phonons. This is demonstrated experimentally with a 3D metamaterial structure fabricated using direct laser writing.